Received: 26 April 2020 | Revised: 13 September 2020 | Accepted: 16 October 2020

DOI: 10.1049/rpg2.12071

IET Renewable Power Generation

The Institution of Engineering and Technology WILEY

ORIGINAL RESEARCH PAPER

Performance evaluation and modelling of the Atir marine current turbine

Eloy Díaz-Dorado[1] | **Camilo Carrillo**[1] | **Jose Cidras**[1] | **David Román**[2] | **Javier Grande**[2]

[1] Electrical Engineering, University of Vigo, EEI – Campus Universitario, Vigo, Spain

[2] Magallanes Renovables S.A., Rua Prego de Montaos, 7, Redondela, Spain

Correspondence
Camilo Carrillo, Electrical Engineering, University of Vigo, EEI – Campus Universitario, Vigo 36310, Spain.
Email: carrillo@uvigo.es

Funding information
H2020 Leadership in Enabling and Industrial Technologies, Grant/Award Number: 730628

Abstract

In this study, the behaviour of a full-size prototype of a platform for tidal energy was analysed. The turbine of this platform is formed by two counter-rotating rotors aligned with the tidal current, such that one rotor is always under the wake of the upstream rotor. The platform was tested under real working conditions; the tidal current was emulated by towing. The results of these tests were used to develop and parameterize a turbine model, which is presented in this paper. The turbine was modelled in terms of power, torque, and thrust coefficients. This model was used to estimate the power curve of the platform and design control strategies that, in addition to maximizing energy production, contribute to the stability of the platform.

1 | INTRODUCTION

Tide is defined as the periodic and alternating rise and fall of the ocean waters caused by the gravitational attraction of the moon and sun. The cyclical nature of the tidal phenomenon causes the generation of marine currents that vary in direction and intensity during a tidal cycle. A crucial difference with respect to other renewable sources is that tides are predictable [1], which makes this energy source very attractive.

To harness that kind of energy, Magallanes Renovables developed a floating system based on a platform that incorporates a submerged part where rotors are installed [2–4]. The platform is designed to be anchored to the sea bottom by four mooring lines. Thus, it does not require any construction on the sea bottom, thereby reducing the typical installation and maintenance costs related to marine energy devices [4].

The platform has a horizontal-axis tidal current turbine, which is arguably the most mature technology in tidal energy systems [5–7]. The turbine is formed by two counter-rotating rotors aligned with the tidal current (from bow to stern or backward), as shown in Figure 1. Both rotors have a variable pitch with a high range of variation, which allows them to change their rotation direction so that it can harvest energy from both tide directions without moving the platform.

Historically, counter-rotating rotors are well known in aviation. Nowadays, modern ships typically use counter-rotating propellers for increased efficiency because the aft propeller recovers some of the rotational energy in the slipstream from the forward propeller. Additionally, this type of propeller has the capability of balancing the torque reaction from the propulsor, which is an essential aspect of torpedoes and other similar propulsion systems [8].

Counter-rotating rotors were used in several wind turbine prototypes [9–13]. Nevertheless, no products are currently mature enough for commercialization. In tidal energy harvesting, there are few examples of systems that use counter-rotating rotors [14–18]. For instance, in [15], a turbine formed by two counter-rotating rotors with the same rotation speed was analysed; in [16], a system was demonstrated with two rotors mounted sideways. These configurations can increase the overall power coefficient [14] or reduce the torque over the supporting structure [17, 18].

A full-size prototype of the aforementioned platform, named Atir, was constructed in a shipyard situated at the "Ria de Vigo" in northwest Spain, where Magallanes Renovables has its headquarters. In this area, no location with enough tidal currents is available to test the platform, so it will be thoroughly tested at the EMEC tidal test site in Scotland (where it is at the time of

This is an open access article under the terms of the Creative Commons Attribution License, which permits use, distribution and reproduction in any medium, provided the original work is properly cited.
© 2021 The Authors. *IET Renewable Power Generation* published by John Wiley & Sons Ltd on behalf of The Institution of Engineering and Technology

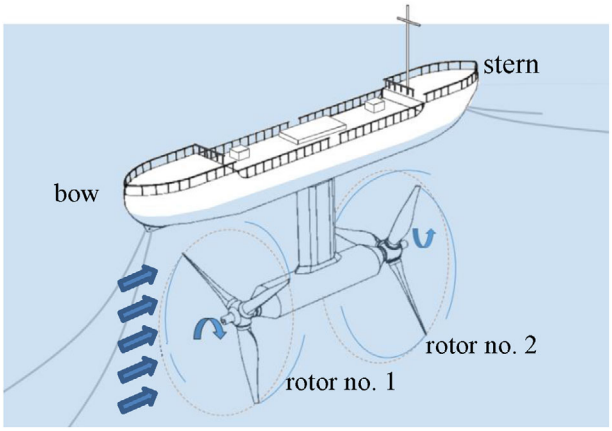

FIGURE 1 Platform configuration

writing this paper) [19]. Before these tests at EMEC, Magallanes set up the systems to check the correct operation of the platform and its capabilities. For this purpose, tidal currents were emulated by towing the platform using a tugboat [14].

The objective of this study was to model the MCT of the Atir platform using data obtained from tests under emulated real working conditions. Given that no data were available from laboratory tests (such as those using flume tanks), several limitations (e.g., the conditions of the tests were not completely controlled) had to be overcome to develop the model.

No previous works presented a model for a full-size tidal converter. The majority of studies focused on numerical simulations [20–22] and laboratory tests of prototypes at a reduced scale [13, 23–25]. In fact, a model setup using measurements in real working conditions for these types of devices has not been published to date. The focus of this study was on modelling the turbine formed by two counter-rotating rotors by using only data collected during the tests that took place at the Ria de Vigo (Spain).

A model that reasonably represents the behaviour of the MCT from the point of view of generation was developed. This model is useful for predicting the behaviour of the MCT in different conditions from those of the tests and for adjusting the control parameters (mainly blade pitch and torque control in the variable speed drives or AC/AC converters). Therefore, different control strategies can be designed to maximize the power generation without affecting the stability of the platform.

In the following sections, the Atir platform and its main components are described. Then, the tests conducted are discussed, and their main results are analysed. Finally, a model of the MCT, which was validated using the measured data, is introduced. Several control possibilities are also evaluated in this section.

2 | FLOATING TIDAL ENERGY PLATFORM

The tidal energy platform, developed by Magallanes Renovables (Spain) and called Atir, consists of a floating platform joined to an MCT formed by two rotors (see Figures 1 and 2). Its main characteristics are listed in Table 1.

FIGURE 2 Platform launching in the harbour of Vigo

TABLE 1 Main characteristics of the full-size prototype

Name	Atir
Rated power	1500 kW
Weight	350 t
Draft/length/breadth	25 m/45 m/6 m
Rotors	2 (counter-rotating)
Rotor diameter/Separation	19 m/1 diameter
Rotor rated speed	17 rpm
Pitch	variable (0° to 270°)
Gearbox ratio	98
Generators	2 × 850 kW @ 690 V
Generators rated speed	1600 rpm
Converters	2 × 900 kW AC/AC

The fundamental advantages of being a floating platform are low maintenance (it has an accessible engine room) and lower installation cost [26]. Given that it is a floating facility, it is adaptable to all sea environments and has little environmental impact.

The platform was designed in such a way (e.g. it features symmetrical shape of the hull, identical rotors etc.) that its behaviour is not affected when the tidal current direction is reversed.

2.1 | Turbine configuration

The MCT is formed by a pair of rotors, one at the bow side and the other one at the stern side. Both rotors have three blades and are designed to rotate in opposite directions (see Figure 1). The rotors can vary their blade pitch from 0° to 270°. Therefore, they can optimize the energy capture under different currents [27], and their rotation direction can be changed according to

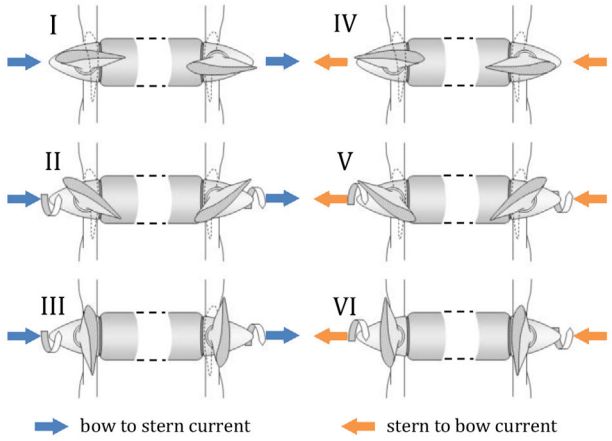

FIGURE 3 Blade pitch positions from feather to optimum pitch position for the two tidal current directions: cases I and IV represent feather position, cases III and VI represent optimum pitch, and cases II and V represent intermediate positions

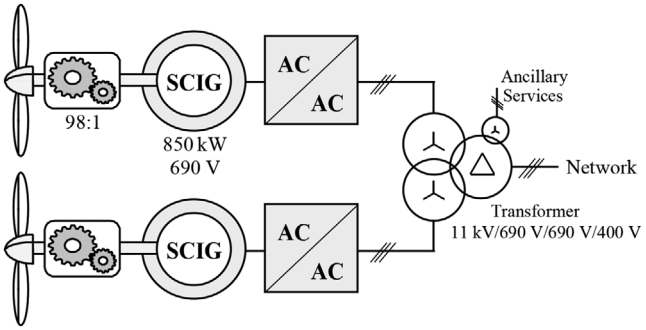

FIGURE 4 Drivetrain configuration

the tide direction, as shown in Figure 3, thus avoiding the movement of the platform.

The rotor hub is located 16 m below the sea level (see Table 1). The rotors are aligned with the tide direction such that when one rotor is upstream with respect to the tidal current direction, the other rotor is downstream.

The rotors are mounted in the same nacelle, which implies a separation of roughly one diameter such that the downstream rotor is strongly affected by the upstream rotor (see Figure 1).

2.2 | Drivetrain

Both rotors have identical drivetrains consisting of a high-speed SCIG [28] mechanically coupled to the rotor through a gearbox (see Figure 4). The energy from the generator is delivered to the power network through a full-power back-to-back AC/AC converter. This type of configuration is widely used in European offshore wind farms [28].

Finally, the outputs of both AC/AC converters are connected to a transformer with four windings, which is shared with the ancillary services. The energy is generated at 690 V and delivered to the distribution network at 11 kV; this MV was selected according to the network conditions at the EMEC site.

2.3 | Clockwise and counterclockwise rotations

The upstream rotor has clockwise rotation, whereas the downstream rotor has counterclockwise rotation (see Figure 1). When the current goes to the bow, the bow rotor is the upstream rotor, whereas the stern rotor is the downstream rotor. When the direction of the current is reversed, the blades of the rotors must rotate in opposite directions. In particular, they must be re-oriented by 180° upon changes in the tide direction.

The rotor blades can rotate by 270° to vary between the full-feathered positions and maximum attack for the two tidal current directions (see Figure 3).

2.4 | Monitoring and control

The platform was monitored and controlled using an SCADA system in which the main variables measured were the following ones:

- Marine current speed using a current speed meter installed on the hull of the platform.
- Platform speed by a GPS (during the towing tests, this value represented the current speed seen by the rotors).
- Torque in the high-speed shaft by means of a torque meter (this value was also estimated by the control software of the AC/AC converter).
- Electrical variables (power, voltage, current etc.) through the control software of the AC/AC converter.

Furthermore, during the tests, the main variables controlled were the following ones:

- Blade pitch position, from 0° to 270°, which allows even changing the rotors' sense of rotation.
- Load torque in the AC/AC converter; when this value is zero, the generator is considered to be unloaded. The load torque was set to different values during the tests.

Data in SCADA were stored during periods of 1, 15, or 30 s depending on the variable. For example, the yaw, pitch, and roll of the platform were stored every second; measurements obtained from variable speed drives (torque, power, rotation etc.) were stored every 15 s; finally, the blade pitch was saved every 30 s.

2.5 | Power network emulation

Owing to the nature of towing tests, it was not possible to establish a connection to the power network. Therefore, the network was emulated using an autotransformer (400 kVA;

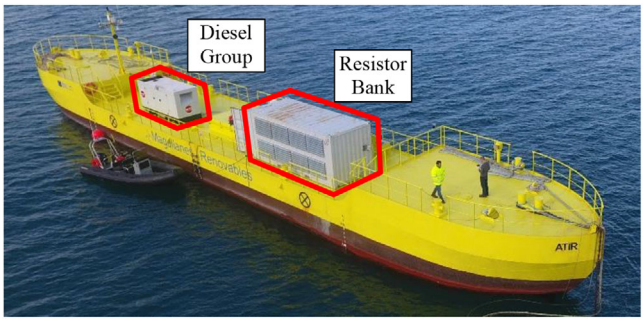

FIGURE 5 Platform with diesel group and resistor bank on board

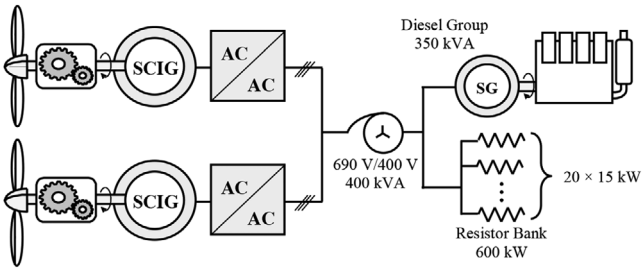

FIGURE 6 Electrical configuration during tests

690 V/400 V), a diesel generator (350 kW), and a bank of dump load resistors (600 kW), as shown in Figures 5 and 6. The value of the resistor bank could be adjusted to match the power generated by the platform, such that the consumption of the diesel group could be optimised.

The objective was to maintain the diesel unit generation at the lowest possible value. To this end, the power injected by the platform matched the power consumed by the resistors by connecting or disconnecting resistor steps. According to the tests conducted on the system, the voltage variation satisfied the limits established in European standards [29]. The frequency variation was higher, but the frequency remained within limits allowed by the power converters.

3 | TOWING TESTS

3.1 | Test conditions

In this paper, the results of the tests in which the tidal current was emulated by towing the platform with a tugboat (see Figure 7 and Table 2) are analysed. The tests were conducted in the Ria of Vigo (Northwest of Spain), where the seabed depth is approximately 40 m. Therefore, it was not expected to interfere with the platform behaviour.

FIGURE 7 Platform towed by a tugboat

TABLE 2 Tugboat main characteristics

Draft/Length/Breadth	4 m/23.4 m/9.8 m
Gross register tonnage	273 t
Power	3752 HP
Bollard pull	54 t
Avg. speed	5.7 knots
Max. speed	11.2 knots

The main objective of these tests was to configure the platform to work in tide conditions and analyse its behaviour. The main differences between these tests and real working conditions under tidal currents are as follows:

1. During tides, the current speed decreases with depth [30]; however, the speed profile during towing is almost constant.
2. Waves act on the platform and tugboat, thereby limiting the test conditions (speed, towing force etc.). They induce oscillations in the towing, and consequently in the moving speed. Note that the period of the waves seen by the platform is affected by its speed.
3. Waves, wind, and marine currents affect the test conditions.
4. During the tests, the towline length was greater than 100 m to minimize the impact of the wake produced by the tugboat (see Figure 7).
5. The emulated tidal current depends on the tugboat operation; therefore, it is affected by the blade pitch and TSR of the rotors. Under real conditions, the current depends only on the tide.
6. The platform showed a certain level of roll, pitch, and yaw during towing (see related discussion in Section 6).

Several variables were measured during the tests. For example, Figure 8 shows the evolution over time for the following variables:

1. GPS speed (knots): Speed of the platform during the tests. This speed was used as freestream current speed because, according to the characteristics of the test site, the existing marine current can be neglected.
2. Power (kW): Power delivered by the generators of both rotors (no. 1 and no. 2).
3. Torque (Nm): Torque of the high-speed shaft of both rotors.
4. Blade pitch (°): Blade pitch of the two rotors.
5. Rot. speed (rpm): Rotation speed of the high-speed shaft of both rotors.

The results show that a power of approximately 400 kW was generated during the tests with a platform speed of approximately 5 knots (2.6 m/s). Note that the achievable speed was limited by the capability of the tugboat, which was strongly dependent on the rotor behaviour and sea conditions.

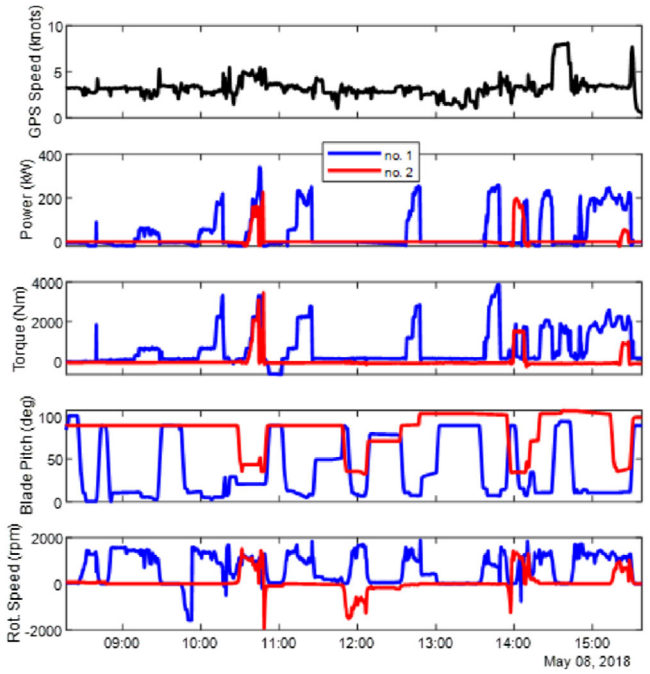

FIGURE 8 Temporal evolution of several variables during towing tests (blue line: rotor no. 1; red line: rotor no. 2)

3.2 | Estimation of feathered and optimum blade pitch positions

The blades were mounted at sea. Then, it was necessary to check the real values of the blade pitch for the full-feathered position and the optimum one that maximizes the power coefficient.

The blade pitch for the optimum power coefficient is the pitch at which, for a given marine current, the maximum power is generated. It is difficult to obtain because the speed of the tugboat depends on the behaviour of the rotors for a given speed and blade pitch, so it is affected by the generated power. Therefore, high values of generated power cause a reduction in tugboat speed that complicates the test of the MCT at high current speed and high power.

The data from the tests conducted with only one rotor running and at different values of current speed, blade pitch, and generated power were used to obtain the map of pitch, TSR, and power coefficient values shown in Figure 9. The same information but changing the main axes can be seen in Figure 10. From these figures, the optimum pitch position can be approximately obtained; its value is 7°. This is the mean value of the pitch angle values at which the highest power coefficient values at the generator side (c_{pg}) were achieved.

The full-feathered position refers to the blade position at which the rotor does not rotate at different current speeds. Its value is between 92° and 94°. This value was estimated through tests in which the rotor was not rotating and was unloaded. Initially, the blade pitch was set to a value that was slightly higher than the supposed full-feathered position. At this moment, the blade pitch was smoothly increased and the value prior to that where the rotor started to rotate was supposed to be the full-feathered position. As an example, data from one of the tests are shown in Figure 11.

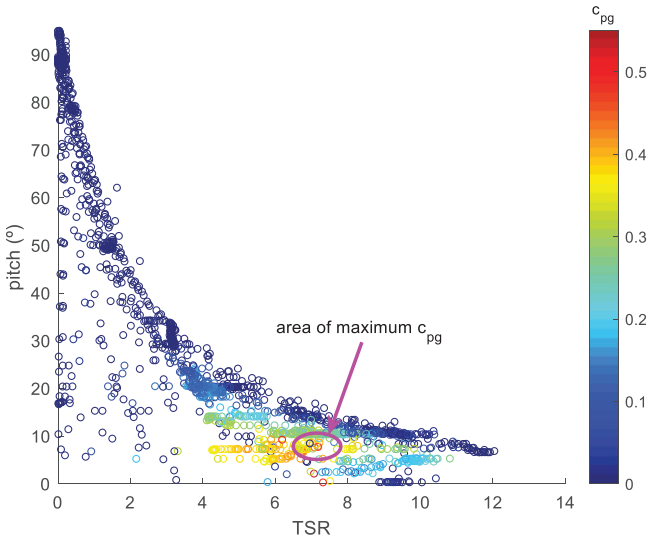

FIGURE 9 Blade pitch angle (and power coefficient at the generator side c_{pg}) for different TSR values

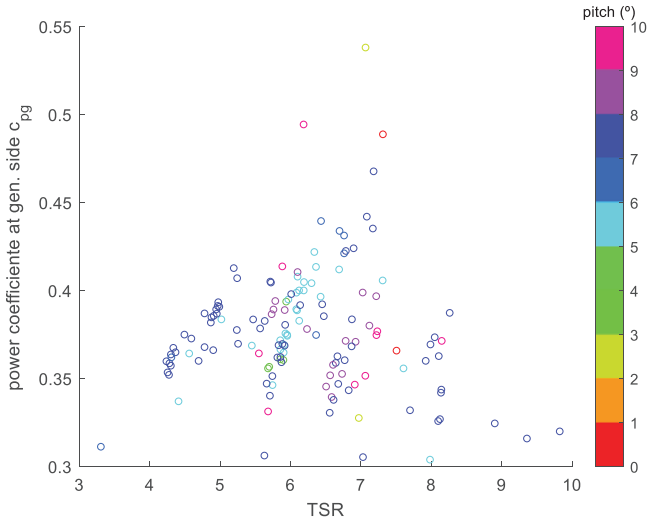

FIGURE 10 Power coefficient at the generator side (c_{pg}) (and blade pitch angle) for different TSR values

4 | ROTOR AND DRIVETRAIN MODELLING

The main relationships between power (P_r), torque (Q_r), and thrust (T) in a rotor can be expressed as follows [31]:

$$P_r = \frac{1}{2}\rho c_{pr} A v^3 Q_r = \frac{1}{2}\rho c_{qr} A v^2 RT = \frac{1}{2}\rho c_t A v^2 \quad (1)$$

where A and R are the area and radius of the rotor, respectively; ρ is the fluid density; v is the current speed; and c_{pr}, c_{qr}, and c_t are the power, torque, and thrust coefficients, respectively.

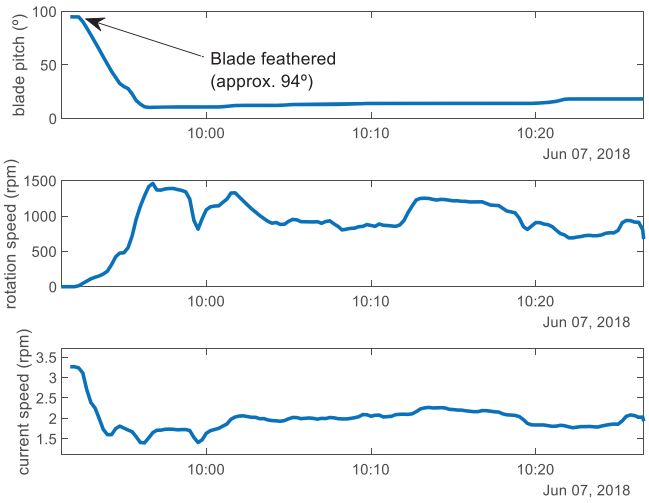

FIGURE 11 Evolution of one rotor from the full-feathered position

The previous equations can be used when only one rotor is running. When both rotors are working, the running conditions of the upstream rotor (referred to as rotor no. 1) affect the downstream rotor (referred to as rotor no. 2) due to wake. Furthermore, the current was measured at one point of the platform that was not affected by rotor turbulences. Therefore, it is considered representative of the freestream current. Accordingly, the parameters of rotor no. 2 were calculated using that current, so they are apparent values. The TSR for both rotors is calculated using the following equations:

$$\mathrm{TSR}_1 = \frac{\omega_1 R}{v_\infty} \tag{2}$$

$$\mathrm{TSR}_{2a} = \frac{\omega_2 R}{v_\infty} \tag{3}$$

where v_∞ is the freestream current speed in m/s; R is the radius rotor in m; ω_1 and ω_2 are the rotor speeds of *the* upstream and downstream rotors in rad/s, respectively; TSR_1 is the tip speed ratio in rotor no. 1; and TSR_{2a} is the apparent TSR value in rotor no. 2. Similarly, the power coefficient in rotor no.1 (c_{pr1}) and the apparent power coefficient in rotor no. 2 (c_{pr2a}) can be defined as follows:

$$c_{pr1} = P_{r1} / \frac{1}{2}\rho A v_\infty^3 \tag{4}$$

$$c_{pr2a} = P_{r2} / \frac{1}{2}\rho A v_\infty^3 \tag{5}$$

where P_{r1} and P_{r2} are the powers in rotors 1 and 2, respectively. Finally, another parameter of interest is the torque coefficient:

$$c_{qr1} = Q_{r1} / \frac{1}{2}\rho R A v_\infty^2 \tag{6}$$

$$c_{qr2a} = Q_{r2} / \frac{1}{2}\rho R A v_\infty^2 \tag{7}$$

where Q_{r1} and Q_{r2} are the torques in rotors 1 and 2, respectively; c_{qr1} is the torque coefficient in rotor no. 1; c_{qr2a} is the apparent torque coefficient in rotor no. 2; and R is the rotor radius. Regarding the thrust force, it can be defined from the thrust coefficient in rotor no. 1 (c_{t1}) and the apparent thrust coefficient in rotor no. 2 (c_{t2a}) as follows:

$$c_{t1} = T_1 / \frac{1}{2}\rho A v_\infty^2 \tag{8}$$

$$c_{t2a} = T_2 / \frac{1}{2}\rho A v_\infty^2 \tag{9}$$

where T_1 and T_2 are the thrust forces in rotors 1 and 2, respectively.

The total power of the MCT at the rotor side can be related to a platform power coefficient (c_{prP}) defined as follows:

$$c_{prP} = c_{pr1} + c_{pr2a} = \frac{P_{r1} + P_{r2}}{\frac{1}{2}\rho A v_\infty^3} \tag{10}$$

In addition to the power, the total rotor torque over the platform affects the behaviour of the platform, for example through its impact on the platform roll (see Section 6). This can be related to the torque over each rotor (it must be considered that they have counter-rotation) by means of the following expression:

$$c_{qrP} = c_{qr1} - c_{qra} = \frac{Q_{r1} - Q_{r2}}{\frac{1}{2}\rho A v_\infty^2} \tag{11}$$

where c_{prP} is the platform torque coefficient at the rotor side.

According to the previous definitions, the performance of the rotor in terms of maximum torque, maximum power, or minimum thrust is more easily analysed in terms of the power, torque, and thrust coefficients. Therefore, these coefficients, as previously defined, were used to model the rotor.

The measurement data from the tests were used to obtain the values of these coefficients. However, most of the measurements were conducted in the power converter and high-speed shaft. Consequently, to estimate the rotor behaviour, it was necessary to consider the performance in terms of the losses in the generators, gearboxes, and AC/AC converters [32], whose models are presented in the following sections.

4.1 | Gearbox performance

The platform has two gearboxes (see Figure 4) mounted between each rotor (low-speed shaft) and the generator (high-speed shaft). The gearbox has a gear ratio of 1:98. The loss data provided by the manufacturer are shown in Table 3.

The power losses can be obtained from the torque losses at different rotor speeds. The resulting data were fitted using the

TABLE 3 Gearbox characteristics

Rotor speed [rpm]	Losses as input torque [kN m]	Oil sump temperature [%]	Losses [%]
0.2	137.6	−33	12.7
0.3	125.3	−16	11.6
0.4	114.7	−14	10.8
0.7	130.0	−17	12.0
0.7	122.7	−14	11.4
1.4	137.7	−18	12.7
1.4	104.9	−14	9.9
4.2	54.3	−9	5.7
4.2	46.8	−8	5.1
4.5	26.5	14	3.4
8.7	31.5	14	3.8
12.1	24.3	17	3.2
15.6	17.8	18	2.7
17.3	15.0	19	2.5
19.8	13.4	20	2.3
20.0	13.3	30	2.3
20.0	9.3	32	2.0

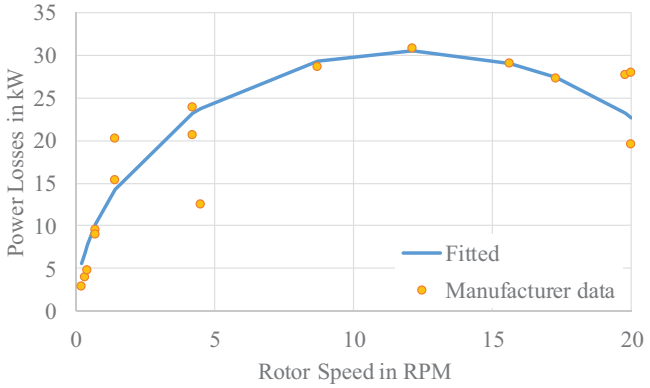

FIGURE 12 Power losses in the gearbox

following equation (see Figure 12):

$$P_{\mathrm{gbl}} = \sqrt{30.5^2\left(1 - \frac{(30\omega/\pi - 12)^2}{12^2}\right)} \tag{12}$$

where ω is the rotor speed in rad/s and P_{gbl} denotes the gearbox power losses in kW.

4.2 | Generator performance

The platform uses one asynchronous generator for each rotor (see Figure 4); its data can be seen in Table 4. According to the data provided by the manufacturer, the generator performance depends on the speed and torque load, as shown in Table 5.

TABLE 4 Data of generator

Brand	ABB
Type	Asynchronous
Rated power	850 kW
Rated torque	5411 Nm
Rated speed	1500 rpm
Max. performance	97.9%

TABLE 5 Generator power losses in kW

	Torque/rated torque [%]				
Speed [rpm]	4%	16%	36%	64%	100%
300	6.3	6.3	6.3	6.3	6.3
600	7.8	7.9	7.9	7.9	8.0
900	9.7	9.7	9.8	10.1	10.9
1200	11.7	11.8	12.2	13.5	16.1
1500	13.9	14.2	15.5	19.1	27.0

4.3 | Performance of generator and gearbox

The power available in a rotor can be obtained from the generator power (measured by the AC/AC converter) and the performance values for the generator and gearbox as follows:

$$P_{\mathrm{r}} = \frac{P_{\mathrm{g}}}{\eta_{\mathrm{gb}}\eta_{\mathrm{g}}} \tag{13}$$

where P_{r} is the power in the rotor; P_{g} is the power in the generator; η_{gb} is the gearbox performance; and η_{g} is the generator performance. From the power values in the rotor and generator, and the measurements in the marine current, the power coefficient in the rotor (c_{pr}) and the generator (c_{pg}) can be obtained using the following equation:

$$c_{\mathrm{pr}} = \frac{c_{\mathrm{pg}}}{\eta_{\mathrm{gb}}\eta_{\mathrm{g}}} \tag{14}$$

where $P_{\mathrm{g}} = \frac{1}{2}\rho c_{\mathrm{pg}} A v_{\infty}^3$.

The power coefficient values shown above were obtained using measurements from only the upstream rotor to overcome the influence over the downstream rotor. The resulting values are shown in Figure 13. Note that the tests were conducted at a power below 50% of the platform rated power. Accordingly, the rotor speed was also below 50% of the rated speed. In this situation, the performance values of the generator and gearbox were approximately 70% and 90%, respectively. The estimated

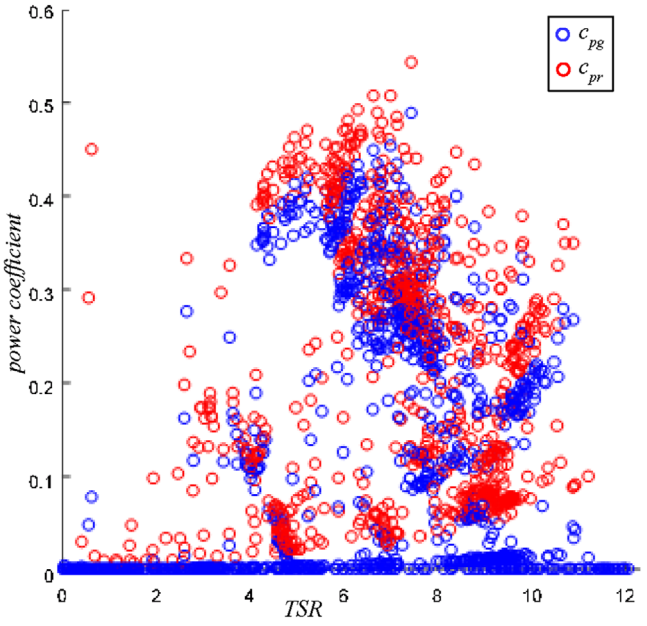

FIGURE 13 Power coefficient at the rotor (c_{pr}) and generator (c_{pg}) sides

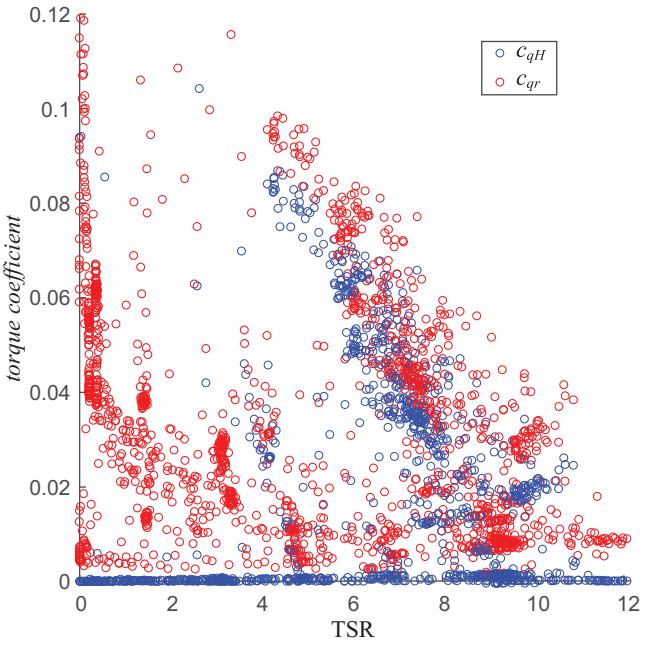

FIGURE 14 Torque coefficient at the rotor (c_{qr}) and high-speed shaft (c_{qH}) sides

maximum value for the power coefficient at the generator side was approximately 0.5.

The rotor torque (Q_r) can be obtained from the torque values Q_H in the high-speed shaft, where the torque meter was installed, and from the estimation of the gearbox losses (Q_{bgl}):

$$Q_r = Q_H + Q_{gbl} \tag{15}$$

where $Q_H = \frac{1}{2}\rho c_{qH} A v_\infty^2$, and c_{qH} is the coefficient torque obtained from the torque at the high-speed shaft. The torque coefficient at the rotor (c_{qr}) can be estimated using these data, yielding the values shown in Figure 14, where the maximum estimated value at the generator side is 0.12.

The rotor torque when the generator is running under no load is equal to the gearbox losses plus the no-load losses of the generator. Note that, for speeds below 1.5 rpm at the low-speed shaft (see Table 3), the gearbox losses lie between 100 and 150 kNm. Nevertheless, other mechanical elements, such as seals and bearings, were not taken into account. Thus, to start the rotor, a torque higher than 150 kNm is necessary.

Similarly, the mechanical power at the rotor when the generator is running under no load is the no-load power at the generator plus the power losses at the gearbox. According to the measurements, the overall no-load power in the drivetrain is in the range 30–40 kW.

4.4 | Losses at AC/AC drive

According to the measurements (see Figure 15), the converter losses are in the range 15–25 kW for generated power levels up to 340 kW (40% of the rated power) and a generator speed

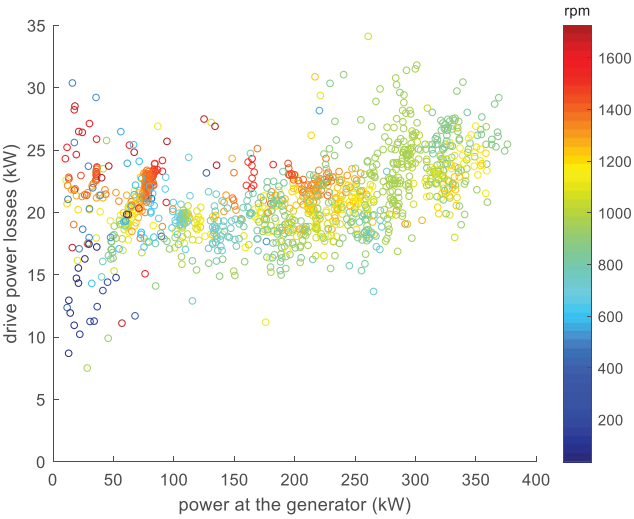

FIGURE 15 Converter power losses versus power and rotation speed of the generator

up to 1600 rpm. These values are close to those given by the manufacturer for the relevant running conditions.

4.5 | Rotor modelling

From a dimensional analysis of the blades, in which eighteen blade sections were considered, the rotor was modelled using the blade element momentum (BEM) method [6, 7, 33, 34, 20] implemented in XFOIL [30, 35, 23] and MATLAB [36]. A detailed flowchart of the process is provided in Appendix 11.

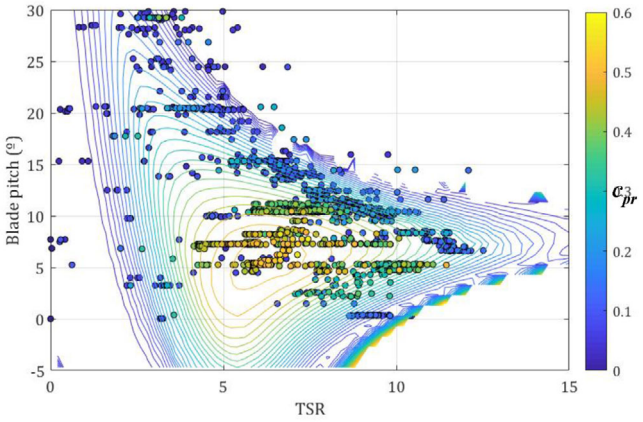

FIGURE 16 Values of c_{pr} as a function of the TSR and blade pitch

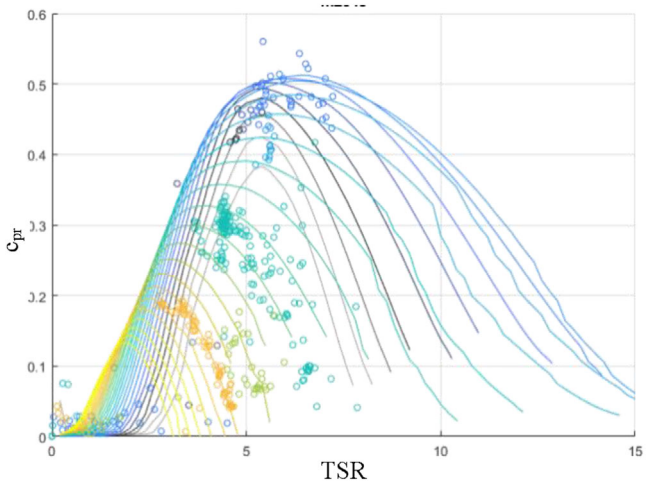

FIGURE 17 Values of c_{pr} as a function of the TSR and blade pitch

Curves were obtained for the power coefficient c_{pr} (see Figures 16 and 17), torque coefficient c_{qr} [37] (see Figures 18 and 19), and thrust coefficient c_t (see Figure 20). These coefficients were calculated at different values of the blade pitch, TSR, and Reynolds numbers [21]. The figures show coloured contour lines with numerical values indicated in the colour bars.

As an example of application of the resulting model, the estimated value for the maximum rotor power coefficient ($c_{pr,max}$) was 0.52 for a pitch angle of 7° and TSR of 6.8. Under these conditions, the torque coefficient (c_{qr}) was 0.082 and the thrust coefficient (c_{tr}) was 1.1.

The rotor model was validated through measurement data from the upstream rotor and from tests with only one rotor running, so the wake effect between rotors did not have to be considered. For this purpose, the coefficients c_{pr}, c_{qr}, and c_t were obtained by taking into account the models for the drivetrain components shown in the previous sections. The values obtained from the measurements are represented by coloured points Figures 16–20.

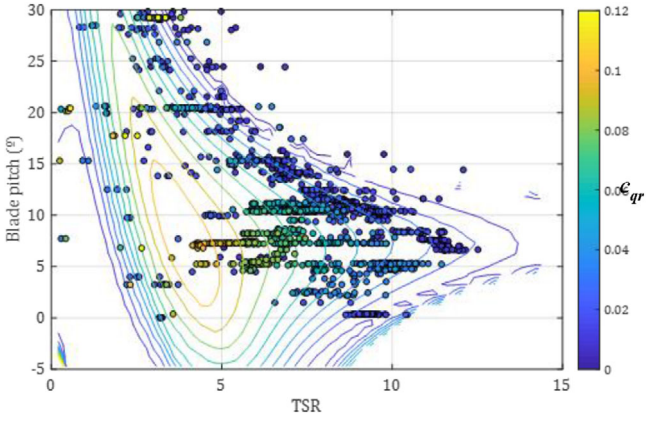

FIGURE 18 Values of c_{qr} as a function of the TSR and blade pitch

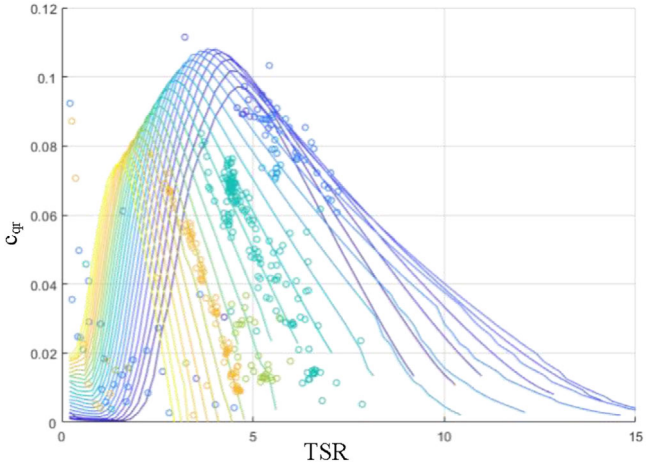

FIGURE 19 Values of c_{qr} as a function of the TSR and blade pitch

As an example, Figure 21 includes the results from one test with emulated tidal current carried out at Ría de Vigo when only one rotor was running. This figure shows the power generated during the test; the values near zero are omitted. From this power, the power coefficient values (c_{pr}) were calculated

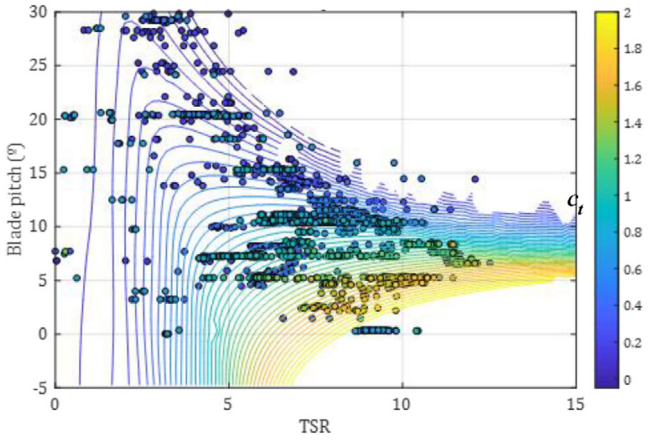

FIGURE 20 Values of c_t as a function of the TSR and blade pitch

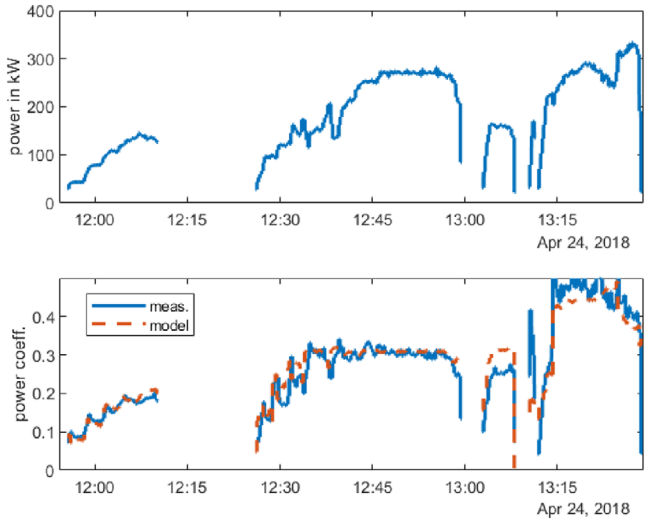

FIGURE 21 Power generated (above) and power coefficient (below) during one of the test with emulated tidal current

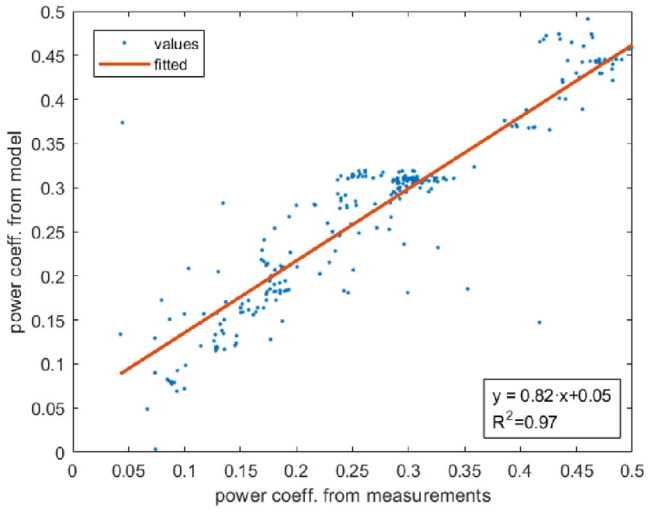

FIGURE 22 Power coefficient from measurements versus power coefficient from model

according to the measurements and the rotor model described above. To evaluate the agreement between the values obtained from the model and those obtained from measurements, both sets are represented in Figure 22 and fitted by means of linear regression (see the resulting equation in the figure). Note that there is a good agreement with respect to the model (coefficient of determination $R^2 \approx 0.97$) with a relative error below 20%.

The most important conclusion of this section is that the measured values reasonably agree with the predicted values using the rotor model.

In the following sections, we analyse the model for the two rotors running simultaneously and the wake effect between them taken into consideration.

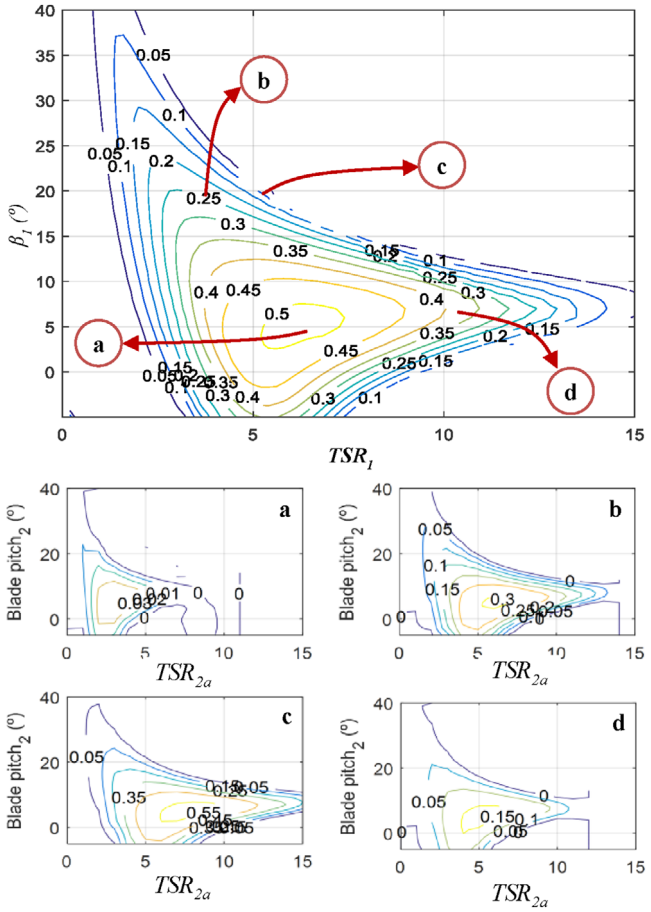

FIGURE 23 Achievable c_{pr1} (main figure) and c_{pr2a} (cases (a) to (d)) values for different working conditions of rotor no. 1

4.6 | Counter-rotating turbine

As mentioned in previous sections, the turbine of the platform is composed of two counter-rotating rotors (the model for a single rotor is shown in Section 4.5) mounted on the same axis and having the same swept area. Depending on the direction of the tide current, while a rotor is upstream (or downstream), the other one is downstream (or upstream). In any case, to analyse the behaviour of the complete turbine, the wake effect between rotors must be considered [12].

By using the model of the upstream rotor, we calculated the wake effect at a distance of one rotor diameter ($1 \times D$), at the location of the downstream rotor (see Appendix 10). Once the wake effect was obtained, the rotor behaviour of the downstream rotor could be calculated.

During the calculations, we considered a set of TSR values from 0 to 15 with a step equal to 0.2, and a set of pitch angles from $-5°$ to $40°$ with a step of $1°$. This means solving 3×10^6 working scenarios for the turbine, taking into account that only generating situations were considered.

As an example of application of the resulting model, Figure 23 represents the achievable power coefficient values in rotor no. 2 (c_{p2a} as a function of TSR_{2a} and β_2) for different working conditions of rotor no. 1 defined by TSR_1, β_1, and c_{p1}.

According to the values shown in Figure 23, when rotor no. 1 is running at its maximum power coefficient, the maximum power coefficient values achievable in rotor no. 2 are lower than 0.03. As an example, this is shown in case a for $TSR_1 = 7$ and $\beta_1 \approx \beta_{opt} = 7°$, where β_{opt} is the pitch angle at which the maximum power coefficient values can be reached. The main reason for this is that the current speed at rotor no. 2 is significantly affected by rotor no. 1. However, when rotor no. 1 is running at higher blade pitch values (see case b with $\beta_1 \approx 20°$, $c_{p1} \approx 0.25$), the value of c_{p2a} can reach up to 0.3. As an example of extreme situation (see case c), the power coefficient of rotor no. 2 can be maximized ($c_{p2a} > 0.5$) for a blade pitch of rotor no. 1 of approximately 20° ($\beta_1 \approx 20°$, $TSR_1 = 5$).

In any case, most of the previous studies analysed the wake effect only when the upstream turbine was at its optimum blade pitch and for the maximum power coefficient. However, the maximum platform power is achieved when both rotors share the total power [9]. This implies that neither the upstream rotor nor the downstream rotor work at its optimum pitch, as will be shown in the following sections.

5 | CHARACTERIZATION OF THE TURBINE

In this section, the behaviour of the turbine of the MCT, which is formed by two counter-rotating rotors (see Section 2), is analysed. First, the influence between both rotors is assessed. Note that the downstream rotor is always affected by the wake of the upstream rotor. Next, the power, torque, and thrust coefficients are estimated considering this effect. Finally, several considerations of the control possibilities of the turbine are analysed.

5.1 | Considerations of the effect of the upstream rotor on the downstream rotor

Figure 24 shows the TSR for the upstream (TSR_1) and downstream (TSR_{2a}) rotors when the downstream rotor was running under no load at a given current speed. For low blade pitch values (below 20°) of the upstream rotor (β_1), the TSR of the downstream rotor (TSR_{2a}) is significantly reduced from 9 to 4. The lowest value was reached when the upstream blade pitch was at its optimum value.

The reduction in the apparent downstream TSR was due to the decrease in the rotor speed. However, the effective reduction could be compensated by the fact that the stream current seen by the downstream rotor was also lowered owing to the wake effect induced by the upstream rotor.

According to this behaviour, during the tests with a constant torque in the downstream rotor set to 1500 Nm, its delivered power was reduced by approximately 17%, from 217 to 178 kW, when the upstream blade pitch was modified. Concerning the downstream apparent power coefficient (c_{pr2a}), its value was lowered by approximately 30%, from 0.3 to 0.21, and the TSR (TSR_{2a}) by approximately 20%, from 7.5 to 6.

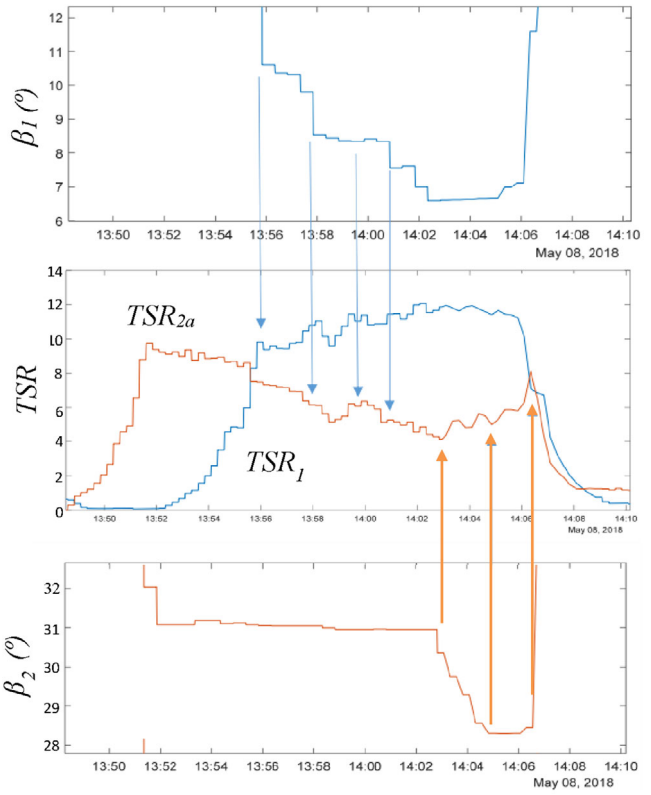

FIGURE 24 Evolution of TSR of upstream (no. 1) and downstream (no. 2) rotors under blade pitch variations with the downstream generator running under no load

Consequently, it was necessary to consider the simultaneous behaviour of the two rotors to obtain the turbine model. This is explained in the following section.

5.2 | Power coefficients of the upstream and downstream rotors and platform

The maximum generation of the platform was achieved when, for a given marine current, the total power extracted by the two rotors reached its maximum value. This situation can be evaluated using the platform power coefficient (c_{prP}) (see Equation (10)), which takes into account the overall energy extracted by the two rotors under certain marine current conditions.

The power coefficient of a turbine formed by two rotors is usually higher than that of a turbine formed by a single rotor. However, the advantages of this configuration are more closely related to other running characteristics, such as torque balancing [11, 38, 24]. In this section, the values of the platform power, torque, and thrust coefficients are estimated and compared with the results obtained during the tests.

To derive the model of the MCT of the platform in terms of power, torque, and thrust coefficients, the wake effect on rotor no. 2 had to be considered. Therefore, the following procedure was carried out:

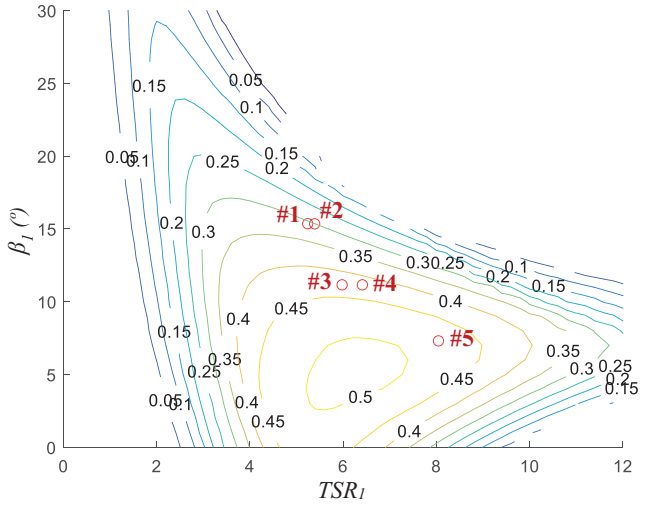

FIGURE 25 Power coefficient in rotor no. 1 (c_{p1}) (values obtained from measurements are included as points marked with #)

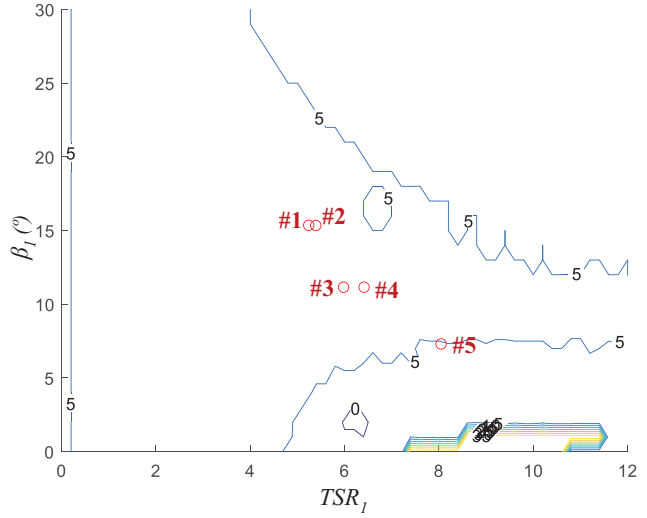

FIGURE 26 TSR values of rotor no. 2 (TSR_{2a}) that maximize the apparent power coefficient of rotor no. 2 (c_{p2amax}) for given working conditions of rotor no. 1 (values obtained from measurements are included as points marked with #)

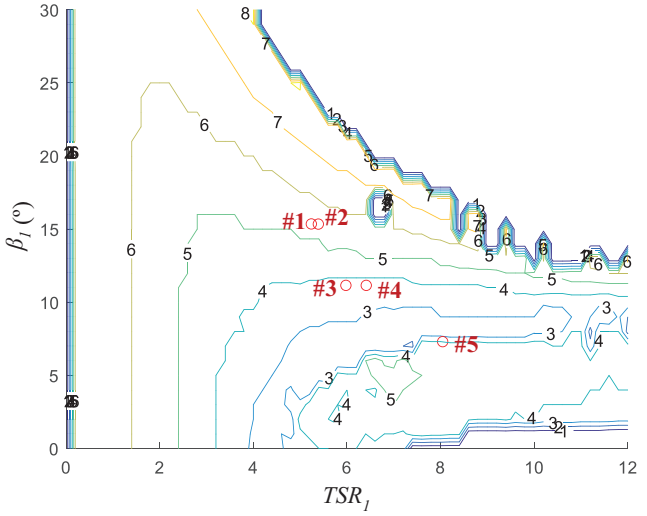

FIGURE 27 Blade pitch values of rotor no. 2 (β_2) that maximize the apparent power coefficient of rotor no. 2 (c_{p2amax}) for given working conditions of rotor no. 1 (values obtained from measurements are included as points marked with #)

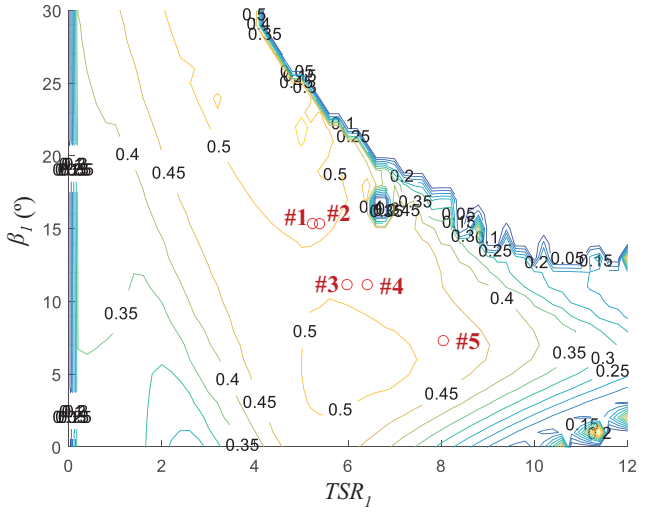

FIGURE 28 Maximum platform power coefficient values ($c_{p1} + c_{p2amax}$) for given working conditions of rotor no. 1 (values obtained from measurements are included as points marked with #)

1. The power coefficient for rotor no. 1 c_{p1} is calculated for different running conditions (defined by TSR_1 and β_1), as shown in Figure 25.
2. For every running condition on rotor no. 1, the working conditions on rotor no. 2 are calculated. This maximizes the apparent power coefficient of rotor no. 2 (c_{p2amax}). Therefore, for every TSR_1-β_1 pair, the corresponding TSR_{2a} (see Figure 26) and β_2 (see Figure 27) are obtained.
3. As a result, for a given TSR_1-β_1 pair, the maximum platform power coefficient values ($c_{prP} = c_{pr1} + c_{pr2a,max}$) are obtained with their corresponding TSR_{2a} and β_1 values, as shown in Figure 28.

Note that the maximum platform power coefficients are easily achieved when the upstream rotor operates at pitch angles higher than the optimum one [12].

A similar procedure was followed to obtain the platform torque coefficient, which, in this case, is defined as $c_{qrP} = c_{qr1} - c_{qr2}$ and represents the torque balance between the rotors (see Figure 29). Similarly, the thrust coefficient sum represents the overall thrust of the platform (see Figure 30).

In the figures mentioned above, a set of points (#1 to #5) obtained from measurements is represented as an example. The values of these points are listed in Table 6. Note that the coefficient values from the model are similar to those obtained from the measurements. For example, in point #2, the values for

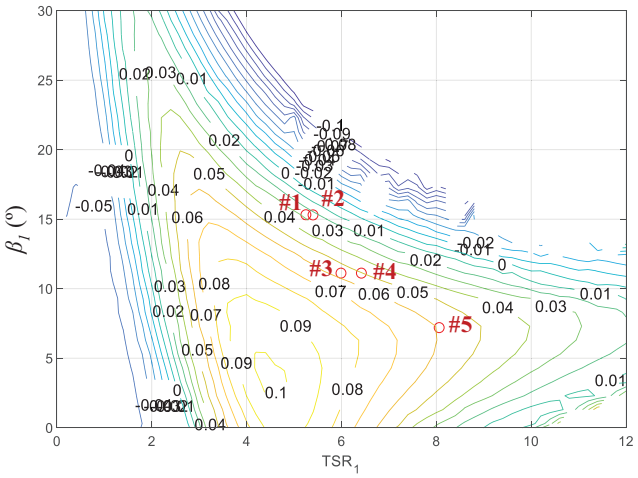

FIGURE 29 Torque coefficient difference ($c_{q1} - c_{q2a}$) for given working conditions of rotor no. 1 and for maximum power coefficient (c_{p2max}) of rotor no. 2 (values obtained from measurements are included as points marked with #)

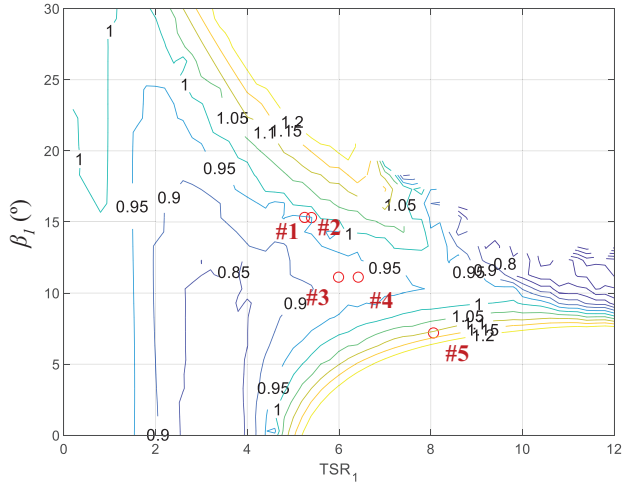

FIGURE 30 Thrust coefficient sum ($c_{t1} + c_{t2}$) for given working conditions of rotor no. 1 and for maximum power coefficient (c_{p2max}) of rotor no. 2 (values obtained from measurements are included as points marked with #)

the model are roughly $c_{pr1} \approx 0.3$; $TSR_{2a} \approx 0.5$; $\beta_2 \approx 5$–6; and $c_{prP} \approx 0.5$. These values are close to those in Table 6.

Finally, note that the maximum platform coefficient can be obtained in a wide range of working conditions of rotors no. 1 and no. 2. This enables the design of different control strategies to maximize the energy production.

5.3 | Considerations of the platform control strategy

As shown in the previous section, for a given stream current, it is possible to achieve a platform power coefficient of approximately 0.5 (see Figure 28). This value can be reached under different running conditions of rotors no. 1 and no. 2 (see Table 6).

TABLE 6 TSR and c_p values obtained from measurements during tests

#	TSR_1	β_1 (°)	c_{pr1}	TSR_{2a}	β_2 (°)	$c_{pr2a,max}$	$c_{prP} = c_{pr1} + c_{pr2a,max}$
1	5.25	15.32	0.26	4.85	6.61	0.25	0.51
2	5.40	15.31	0.27	4.91	6.59	0.25	0.51
3	5.99	11.12	0.36	3.93	7.70	0.15	0.51
4	6.42	11.12	0.36	3.80	7.70	0.14	0.50
5	8.06	7.20	0.45	3.40	7.57	0.06	0.51

TABLE 7 Running values for point #2

Rotor no. 1	Rotor no. 2				
TSR_1	5.40	TSR_{2a}	4.91		
β_1 (°)	15.31	β_2 (°)	6.59	Total	
c_{pr1}	0.27	$c_{pr2a,max}$	0.22	$c_{pr1} + c_{pr2a,max}$	0.49
c_{q1}	0.050	c_{q2a}	0.045	$c_{q1} - c_{q2a}$	0.005
c_{t1}	0.35	c_{t2a}	0.56	$c_{t1} + c_{t2a}$	0.91

In this context, it is possible to maximize the power delivered by the platform and achieve another objective simultaneously. For example, to minimize the roll of the platform, it would be desirable that both rotors have a similar torque, considering that they have counter-rotation. The torque can be balanced when both torque coefficients are similar.

As an example, Table 7 shows the running values estimated for point #2 in Table 6. The platform power coefficient is close to 0.5, and the torque coefficients of rotors no. 1 and no. 2 (c_{qr1} and c_{qr2a}) are similar.

5.4 | Platform power curve

Using the model presented in the previous section, an estimated power curve of the MCT can be obtained, as shown in Figure 31. The power delivered at the MV side of the platform was obtained by estimating losses in gearboxes, generators, AC drives, and transformers.

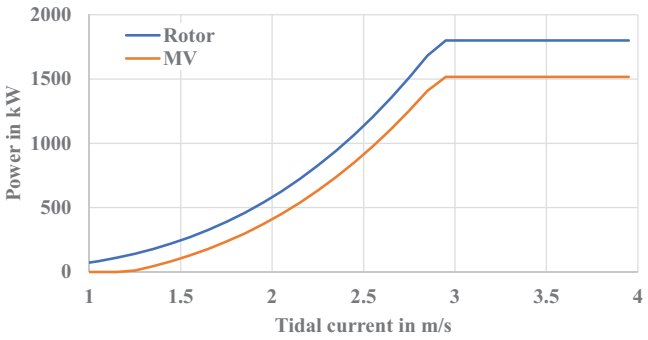

FIGURE 31 MCT power curve at the rotor side and at the MV side

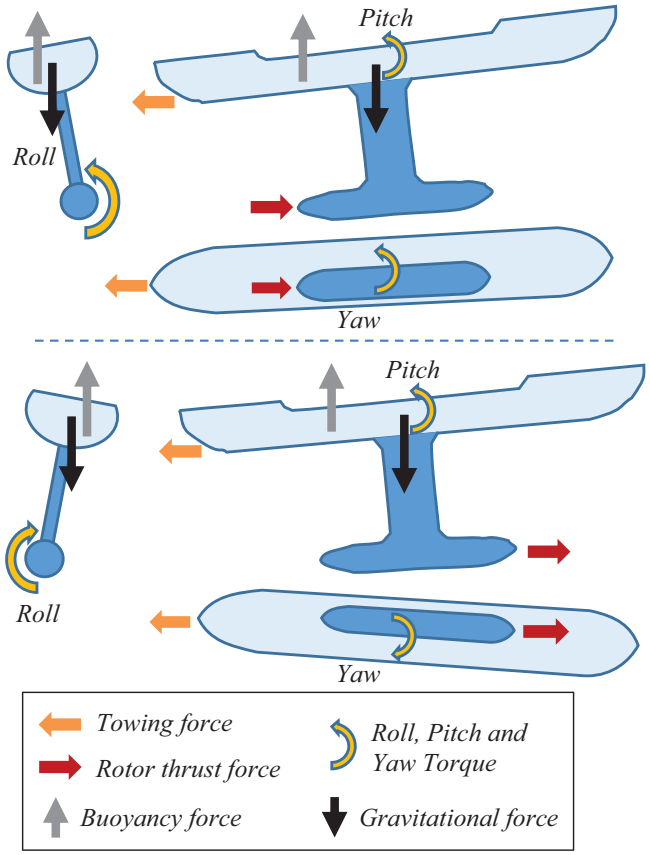

FIGURE 32 Roll, pitch, and yaw of platform associated with torques in upstream (upper) and downstream (lower) rotors

The following values were obtained: the cut-in current speed was approximately 1 m/s; the rated current speed was approximately 2.9 m/s; and the rated power was 1500 kW at the MV side.

The energy produced by the MCT can be estimated using this power curve. For example, data for the East Coast of Florida (USA) available in the Southeast National Marine Renewable Energy Center [39, 40] can be used. For this site, tidal current data were measured with an acoustic Doppler current profiler for 287 days in 2019. The recorded mean current speed in the depth range of operation of the MCT was 2.2 m/s, reaching a maximum speed of 5.9 m/s. At this site, the estimated energy production at the MV side is 6238 MWh/year with a value of equivalent full-load hours of 4159 h/year.

6 | ROLL, PITCH, AND YAW DURING THE TOWING TEST

When the platform is operating, the torque of the rotor produces the roll of the platform. This roll is related to the torque of the rotor and the metacentric height according to the positions of the centres of buoyancy and gravity (see Figure 32).

The Atir platform has two counter-rotating rotors. When they have the same torque, the roll of the platform is cancelled. When they do not have the same torque, the roll is a function of the torque difference between the rotors. When towed, the platform roll causes a misalignment of the traction forces that induces significant pitch and yaw (see Figure 33). Figure 34 shows different roll values during a test when only one rotor was running; in this case, the relationship between generator torque and roll is clear.

FIGURE 33 Roll and yaw of the Atir platform during tests with only one turbine running

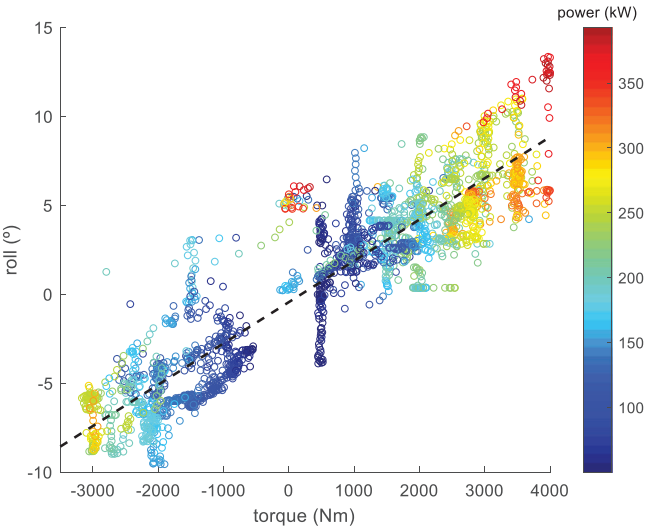

FIGURE 34 Roll values during tests

Apart from mechanical stress on the platform, the roll, pitch, and yaw affect the generation of the turbine (e.g. the effective area seen by the current is reduced when the rotor axis is misaligned with the marine current) or the towing effectiveness (e.g. the towing resistance of the platform is higher when the yaw increases).

The platform pitch is corrected by moving the water between the reservoir tanks placed in the stern and bow. However, this could affect the position of the centre of gravity and, therefore, the overall platform behaviour.

All of the abovementioned aspects must be considered when extrapolating the towing tests to real tidal current conditions.

7 | CONCLUSIONS

The Atir platform is a full-size prototype tidal energy device whose turbine is formed by two counter-rotating underwater rotors aligned with the tidal current. This paper reports an analysis of this platform based on test results and a complete model for its generation system.

The starting point for this study was the results of tests carried out at Ría de Vigo (Spain). During these tests, the platform was towed to emulate tidal currents. Under these conditions, the platform was operated in the same way that under real tidal currents, although with reduced rated power owing to the size of the dump loads.

To achieve the objectives of the study, a complete model for the generation systems was developed. It includes the following elements:

1. Losses in gearboxes, generators, and AC/AC converters.
2. Estimation of the rotor behaviour in terms of the TSR, blade pitch, and power coefficient using BEM techniques. Torque and thrust coefficients are also included.
3. Wake effect of the upstream rotor on the downstream rotor.

Model tuning was performed using real data from the abovementioned tests.

As a result, a model of the MCT of the platform is proposed. It was obtained from tests carried out in real conditions. The control and measured variables are not completely under control in this type of tests. This makes obtaining the model parameters more challenging than in a laboratory. Nevertheless, the proposed model accurately represents the platform in terms of generation and rotor behaviour.

Once the model was obtained, the performance of the platform in terms of the power coefficient was estimated. An approximate value of 0.5 for the MCT was achieved during the tests. In addition, the model allows the analysis of the torque balance between rotors, which affects the platform roll, and the thrust forces by means of their corresponding coefficients.

Furthermore, the behaviour of the Atir platform under different conditions from those of tests was analysed. It was concluded that the use of aligned dual rotors allows operation under a wide range of running conditions while the platform power coefficient is close to its optimum value. In this context, several control strategies can be established, for example, by compensating the roll of the platform through the balance of the torque in the rotors.

Overall, this paper reports an MCT model for a full-scale prototype of a tidal energy platform. This model was used to analyse the behaviour of the platform in terms of energy production, torque, and thrust. Furthermore, the viability of control strategies with multiple objectives (energy, platform stability etc.) was studied.

NOMENCLATURE

a	axial flow induction factor
a'	tangential flow induction factor
c_p	power coefficient
c_q	torque coefficient
c_t	thrust coefficient
v	current speed (m/s)
A	rotor area (m^2)
D	rotor diameter (m)
R	rotor radius (m)
P	power (W)
Q	torque (Nm)
T	thrust force (N)
TSR	tip speed ratio

Abbreviations and names

Atir	name of the full-size prototype
EMEC	European Marine Energy Centre
MCT	marine current turbine
MV	medium voltage
SCADA	supervisory control and data acquisition
SCIG	squirrel cage induction generator

Greek symbols

β	blade pitch (degrees)
ω	rotor speed (rad/s)
ρ	water density (kg/m^3)
η	performance

Subscripts

0	freestream current
1	upstream turbine
2	downstream turbine
a	apparent, it refers to parameters in downstream turbine calculated using freestream (upstream) current speed
e	effective
g	generator
gb	gearbox
i	number of blade section
l	losses
max	maximum value
r	rotor
t	tangential
x	axial
H	high-speed shaft
L	low-speed shaft
P	platform
∞	freestream current

ACKNOWLEDGMENT

This work is part of the project OCEAN_2G, which received funding from the European Union's Horizon 2020 research and innovation programme under grant agreement no. 730628.

ORCID

Eloy Díaz-Dorado https://orcid.org/0000-0002-4247-2167
Camilo Carrillo https://orcid.org/0000-0002-8457-5615

REFERENCES

1. Kavousi-Fard, A.: Modeling Uncertainty in Tidal Current Forecast Using Prediction Interval-Based SVR. IEEE Trans. Sustainable Energy 8(2), 708–715 (2017)
2. Magallanes Renovables. http://www.magallanesrenovables.com (2019). Accessed July 2019
3. National Geographic: 'The Magallanes Project (in Spanish)'. https://www.nationalgeographic.com.es/ciencia/grandes-reportajes/proyecto-magallanes-futuro-esta-energia-las-mareas-energia-mareomotriz_12343/1 (2019). Accessed Sept 2019
4. Chen, H., et al.: Attraction, challenge and current status of marine current energy. IEEE Access 6, 12665–12685 (2018)
5. Ng, K.W., Lam, W.H., Ng, K.C.: 2002-2012: 10 years of research progress in horizontal-axis marine current turbines. Energies 6(3), 1497–1526 (2013)
6. Li, W., et al.: Review on the blade design technologies of tidal current turbine. Renewable Sustainable Energy Rev. 63, 414–422 (2016)
7. Nachtane, M., et al.: A review on the technologies, design considerations and numerical models of tidal current turbines. Renewable Energy 157, 1274–1288 (2020)
8. Molland, A.F. (ed.): The Maritime Engineering Reference Book. Butterworth-Heinemann, Oxford (2008)
9. Lee, S., Son, E., Lee, S.: Velocity interference in the rear rotor of a counter-rotating wind turbine. Renewable Energy 54, 235–240 (2013)
10. Cho, W., et al.: Development and experimental verification of counter-rotating dual rotor/dual generator wind turbine: Generating, yawing and furling. Renewable Energy 114, 644–654 (2017)
11. Lee, S., Kim, H., Lee, S.: Analysis of aerodynamic characteristics on a counter-rotating wind turbine. Curr. Appl. Phys. 10(2 SUPPL.), S339–S342 (2010)
12. Lee, S., et al.: Effects of design parameters on aerodynamic performance of a counter-rotating wind turbine. Renewable Energy 42, 140–144 (2012)
13. Mitulet, L.A., et al.: Wind tunnel testing for a new experimental model of counter-rotating wind turbine. Procedia Eng. 100, 1141–1149 (2015)
14. Clarke, J.A., et al.: Design and testing of a contra-rotating tidal current turbine. J. Power Energy 221, 171–179 (2007)
15. Lee, N.J., et al.: Performance study on a counter-rotating tidal current turbine by CFD and model experimentation. Renewable Energy 79(1), 122–126 (2015)
16. Coiro, D.P., et al.: Development, deployment and experimental test on the novel tethered system GEM for tidal current energy exploitation. Renewable Energy 114, 323–336 (2017)
17. O'Doherty, D.M., et al.: Considerations of improved tidal stream turbine performance using double rows of contra-rotating blades. In: 8th European Wave and Tidal Energy (EWTEC 2009). Uppsala, Sweden, pp. 1–9 (2009)
18. Clarke, J., et al.: Analysis of a single point tensioned mooring system for station keeping of a contra-rotating marine current turbine. IET Renewable Power Gener. 4, 473–487 (2010)
19. EMEC: Grid-connected tidal test site. http://www.emec.org.uk/facilities/tidal-test-site/ (2020). Accessed July 2020
20. Nachtane, M., et al.: Design and hydrodynamic performance of a horizontal axis hydrokinetic turbine. Int. J. Automot. Mech. Eng. 16(2), 6453–6469 (2019)
21. Batten, W.M.J., et al.: Hydrodynamics of marine current turbines. Renewable Energy 31(2), 249–256 (2006)
22. Lam, W.H., Chen, L., Hashim, R.: Analytical wake model of tidal current turbine. Energy 79(C), 512–521 (2015)
23. Goundar, J.N., Ahmed, M.R., Lee, Y.H.: Numerical and experimental studies on hydrofoils for marine current turbines. Renewable Energy 42, 173–179 (2012)
24. Habash, R.W.Y., et al.: Performance of a contrarotating small wind energy converter. ISRN Mech. Eng. 2011, 1–10 (2011)
25. Batten, M.E., et al.: Comparison between CFD simulations and experiments for predicting the far wake of horizontal axis tidal turbines. IET Renewable Power Gener. 4, 613–627 (2010)
26. Zhou, Z., et al.: Developments in large marine current turbine technologies – A review. Renewable Sustainable Energy Rev. 71, 852–858 (2017)
27. Burton, T., Sharpe, D., Junkins, N., Bossanyi, E.: Wind Energy Handbook. John Wiley & Sons, Chichester (2001)
28. Vázquez Hernández, C., Telsnig, T., Pradas Villalba, A.: JRC Wind Energy Status Report - 2016 Edition: Market, technology and regulatory aspects of wind energy. Publications Office of the European Union. Luxembourg (2017)
29. CENELEC: "Voltage characteristics of electricity supplied by public electricity networks, Standard EN 50160:2010." (2010)
30. Batten, W.M.J., et al.: The prediction of the hydrodynamic performance of marine current turbines. Renewable Energy 33(5), 1085–1096 (2008)
31. Johnson, G.L.: Wind Energy Systems. Kansas State University (2006)
32. Li, Y., et al.: Design and test of a 600-kW horizontal-axis tidal current turbine. Energy 182, 177–186 (2019)
33. Benelghali, S., Benbouzid, M., Charpentier, J.-F.: Modeling and control of a marine current turbine driven doubly-fed induction generator. IET Renewable Power Gener. 4(1), 1–11 (2010)
34. Benelghali, S., Benbouzid, M.E.H., Charpentier, J.F.: Generator systems for marine current turbine applications: A comparative study. IEEE J. Ocean. Eng. 37(3), 554–563 (2012)
35. Drela, M., Youngren, H.: XFOIL Subsonic Airfoil Development System. https://web.mit.edu/drela/Public/web/xfoil/ (2019). Accessed July 2019
36. Matlab Release 2018b. The MathWorks Inc., Natwick, MA (2018)
37. Benelghali, S., et al.: Experimental validation of a marine current turbine simulator: Application to a permanent magnet synchronous generator-based system second-order sliding mode. Ind. Electron. 58(1), 118–126 (2011)
38. Rosenberg, A., Selvaraj, S., Sharma, A.: A novel dual-rotor turbine for increased wind energy capture. J. Phys. Conf. Ser. 524(1), 012078 (2014)
39. Southeast National Marine Renewable Energy Center: Moored ADCP: Available Data. http://coet.fau.edu/resource-measurement-modeling/available-data.html (2020). Accessed February 2020
40. Machado, M.C.P., VanZwieten, J.H., Pinos, I.: A measurement-based analysis of the hydrokinetic energy in the Gulf Stream. J. Ocean Wind Energy 3(1), 25–30 (2016)
41. Larsen, G.C.: A Simple Wake Calculation Procedure. Riso National Laboratoy, Riso-M, No. 2760 (1988)
42. Jensen, N.O.: A Note on Wind Generator Interaction. Riso National Laboratoy, Riso-M, No. 2411 (1983)
43. Frandsen, S.: On the wind speed reduction in the center of large clusters of wind turbines. J. Wind Eng. Ind. Aerodyn. 39, 251–265 (1992)
44. Kiranoudis, C.T., Maroulis, Z.B.: Effective short-cut modelling of wind park efficiency. Renewable Energy 11(4), 439–457 (1997)
45. Ahmed, U., et al.: Fluctuating loads on a tidal turbine due to velocity shear and turbulence : Comparison of CFD with field data. Renewable Energy 112, 235–246 (2017)
46. Medici, D., et al.: The upstream flow of a wind turbine: blockage effect. Wind Energy 14(January), 691–697 (2011)

How to cite this article: Díaz-Dorado E, Carrillo C, Cidras J, Román D, Grande J. Performance evaluation and modelling of the Atir marine current turbine. *IET Renew Power Gener.* 2021;15:821–838. https://doi.org/10.1049/rpg2.12071

APPENDIX A: MODELLING OF WAKE EFFECT

To analyse the behaviour of the complete turbine, we had to consider the fact that the rotors are aligned with the tide current. Therefore, the downstream rotor, which can be the stern or bow rotor depending on the tide direction, is under the wake of the upstream rotor. This is usually approximated as an effective reduction of the current speed [41–44]. However, owing to the proximity of the two rotors (see Table 1), a more detailed model had to be used. That model took into account the wake rotation [27, 45, 25], that is, the axial and tangential current speeds induced by the wake in the downstream rotor [12, 22, 46].

If only a rotor is considered, the axial speed ($v_{x,i}$) and the tangential speed ($v_{t,i}$) caused downstream by the rotor blade section i at a distance equal to $1 \times D$ is expressed as follows [12]:

$$\frac{v_{x,i}}{v_\infty} = 1 - 2a_i \tag{A.1}$$

$$\frac{v_{t,i}}{\omega r_i} = 2a'_i \tag{A.2}$$

where r_i is the radius of the rotor blade section i in m; ω is the rotor speed in rad/s; and a_i and a'_i are the axial and tangential flow induction factors, respectively, in m/s. When the downstream rotor is considered, the axial and tangential speeds in the rotor can be written as follows: [46]:

$$\frac{v_{x,i}}{v_\infty} = 1 - a_i\left(1 + \frac{2x}{D}\left(1 + \frac{4x^2}{D^2}\right)^{-\frac{1}{2}}\right) \tag{A.3}$$

$$\frac{v_{t,i}}{\omega r_i} = a'_i\left(1 + \frac{2x}{D}\left(1 + \frac{4x^2}{D^2}\right)^{-\frac{1}{2}}\right) \tag{A.4}$$

where x is the distance to the downstream rotor; for the Atir platform, $x = D$.

Using the above equations, the axial and tangential speeds on the downstream rotor can be obtained, as shown in Figures A.1 and A.2 in which these speeds were calculated for different rotor distances ($1D$ and $2D$). To obtain them, the running conditions shown in Table A.1 were considered.

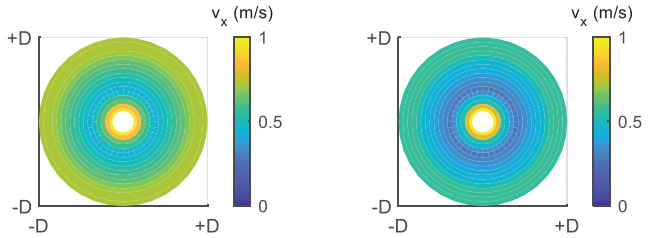

FIGURE A.1 Axial speed (v_x) in a downstream rotor when it is located at a distance 1D (left) and 2D (right)

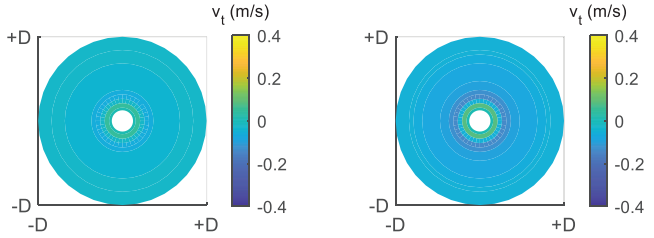

FIGURE A.2 Tangential speed (v_t) in a downstream rotor when it is located at a distance 1D (left) and 2D (right)

TABLE A.1 Running conditions for wake calculation

Rotor	Parameter	Value
—	Free stream current speed (v_∞)	1 m/s
1	Pitch angle (β_1)	17°
1	TSR (TSR_1)	5.2
1	Rotor speed (ω_1)	5.67 rpm
2	Pitch angle (β_2)	13°
2	TSR (TSR_{2a})	4.3
2	Rotor speed (ω_1)	4.19 rpm

Appendix B: MODELLING FLOWCHART

Figure A.3 shows the flowchart of the modelling process. Its main blocks are explained in the following paragraphs.

Xfoil block:

The outputs for this block are as follows:

- Lift coefficient (c_l)
- Drag coefficient (c_d)
- Moment coefficient (c_m)

for different values of parameters:

- Attack angle (α) between $\pm 60°$
- Reynolds numbers (Re) between 10^5 and 10^7
- Blade profiles, which are defined by the distance r to the centre of the rotor, from 1.5 to 9.5 m.

The resulting coefficient values are stored in 3D matrixes.

BEM model for profile blocks:

From the results of the previous block, the following values are obtained:

- Axial flow induction factor a
- Tangential flow induction factor a'
- Attenuation values F
- Gradient factors: lift gradient $\partial L/\partial r$, drag gradient $\partial L/\partial r$, torque gradient $\partial L/\partial r$, power coefficient gradient $\partial c_p/\partial r$ etc.

for different values of parameters:

- Relative current speed v between 0.5 and 17 m/s
- Relative current speed φ direction between $\pm 45°$

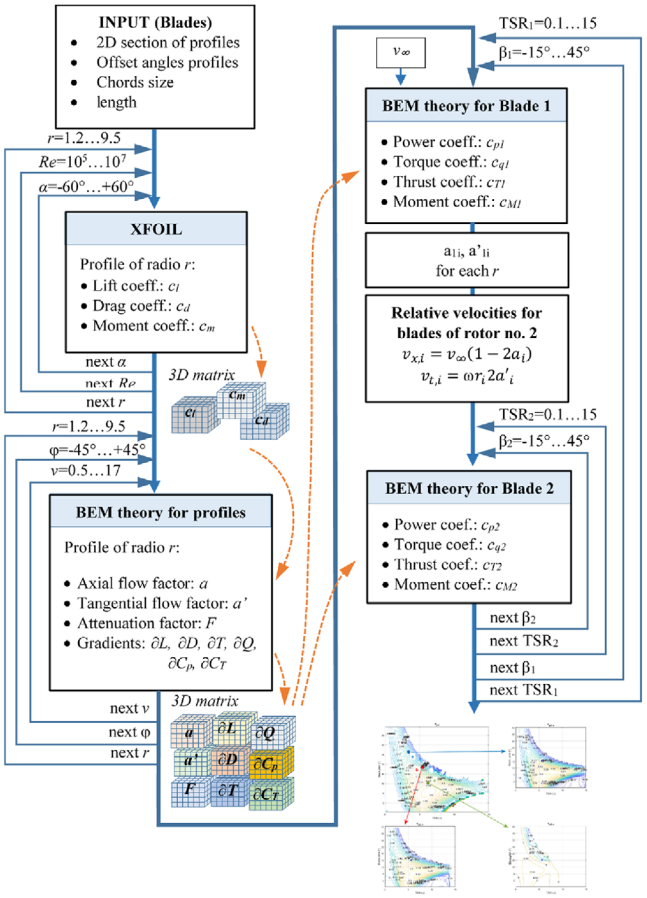

FIGURE A.3 Modelling flowchart

BEM model for blades of rotor no. 1:

From data of the previous block, the coefficient of torque c_q, power c_p, thrust c_T, and torque on the blade axis c_M are obtained for rotor no. 1 for different values of parameters:

- TSR_1 between 0 and 15
- Blade pitch β_1 between −15° and 45°

The values of the axial and radial fluxes (a and a') are used to calculate the impact over the current speed seen by rotor no. 2 due to the wake caused by rotor no. 1.

Wake current speed:

The values of the flow induction factors (a and a') are used to calculate the current speed seen by rotor no. 2, which is affected by the wake caused by rotor no. 1.

BEM model for blades of rotor no. 2:

Using data from previous steps, different coefficients (c_q, c_p, c_T, *and* c_M) are obtained for rotor no. 2. These values are obtained for values between 0 and 15 for TSR_2, and between −15° and +45° for blade pitch β_2. In this case, the relative speed of each profile is different. Thus, the angle φ is obtained using a and a' from rotor no. 1. This implies that, for each pair of TSR_1 and β_1 values, all running conditions of rotor no. 2 must be obtained (TSR_2 between 0 and 15, and β_2 between −15° and 45°).